33rd Annual International Conference of the IEEE EMBS
Boston, Massachusetts USA, August 30 - September 3, 2011

A joint acquisition–reconstruction paradigm for correcting inhomogeneity artifacts in MR echo planar imaging

Joseph C. Dagher and François G. Meyer

Abstract— **One of the main sources of signal degradation in rapid MR acquisitions, such as Echo Planar Imaging (EPI), is magnetic field variations caused by field inhomogeneities and susceptibility gradients. If unaccounted for during the reconstruction process, this spatially-varying field can cause severe image artifacts. In this paper, we show that correcting for the resulting degradations can be formulated as a blind image deconvolution problem. We propose a novel joint acquisition-processing paradigm to solve this problem. We describe a practical implementation of this paradigm using a multi-image acquisition strategy and a corresponding joint estimation-reconstruction algorithm. The estimation step computes the spatial distribution of the field maps, while the reconstruction step yields a Minimum Mean Squared Error (MMSE) estimate of the imaged slice. Our simulations show that this proposed joint acquisition-reconstruction method is robust and efficient, offering factors of improvement in the quality of the reconstructed image as compared to other traditional methods.**

I. INTRODUCTION

In a two-dimensional (2D) slice-selective imaging experiment, the signal induced by an elemental volume $dV \triangleq dxdydz$ in an MRI receiver coil is given by [1]

$$dS \propto f(x,y,z,t) \exp\left\{ i2\pi \Big[xK_x(t) + yK_y(t) + \gamma \int_0^t \Delta B(x,y,z,\tau) d\tau \Big] \right\} \mathrm{d}V \quad (1)$$

where $f(x,y,z,t)$ represents the spatio-temporal distribution of the object, γ is the gyromagnetic ratio (in Hz/T), and $K_x(t)$ and $K_y(t)$ denote the spatial frequencies encoded by the read-out and phase gradients at time t, respectively. The term $\Delta B(x,y,z,t)$ represents any deviation from the desired magnetic field as controlled by the gradients. The sources of these inhomogeneities are either external (e.g., main field or magnetic field gradient inhomogeneities, gradient coil non-linearity), or due to internal differences between the magnetic susceptibility of different materials. The susceptibility-induced inhomogeneities can be very severe, particularly when they arise across air/tissue or air/bone interfaces. For example, in the brain, large susceptibility gradients occur around the anterior-frontal regions, temporal lobes and around the sinuses [2], [3]. In the absence of $\Delta B(x,y,z,t)$, it is clear from (1) that the evolution of the spatial frequencies K_x and K_y with time defines the grid over which measurements are made. In the simple case of a regular rectangular grid, the relationship between the induced signal S and the object f amounts to a simple Fourier transform operation. The inhomogeneities $\Delta B(x,y,z,t)$, however, perturb the effective trajectory of $K_x(t)$ and $K_y(t)$. If unaccounted for during the reconstruction process, this will result in severe image artifacts including twisting in the shape of the ROI (geometric warping) and loss of signal (signal drop) [3]. These degradations can have detrimental effects, especially in tasks that require geometric accuracy, such as registration of fMRI data to brain atlases for activity localization [4]–[6], neurosurgery and computer assisted surgery [7], [8], rigid-body (e.g., cortices) segmentation, etc. Ultimately, this influences the statistical decision about the presence/absence of neuronal activation. Since the inhomogeneity term scales with magnetic field strength and long read-out time, we note that this problem only gets worse with the advent of machines with stronger magnetic fields. Traditional solutions offered in the literature can generally be divided into two classes: acquisition-based and processing-based methods. Acquisition methods modify the pulse sequence to carefully preempt inhomogeneity in specific regions via the careful calibration of gradients [9]–[12]. This only partially corrects for the problem in one region, while increasing artifacts in other regions. Also, the additional pulse sequences often require an increase in the scan time, and place high demand on the shim coils. Processing-based algorithms attempt to reconstruct the object in two distinct steps. First, an estimate of the field maps $\Delta B(x,y,z)$ is computed either via a separate acquisition or from the distorted data itself. Then, the data is unwarped/de-blurred according to the field map estimate using post-processing methods. [3], [13]–[18]. This approach often fails in instances of inhomogeneity-induced signal loss [16], as it becomes very difficult to (a) estimate inhomogeneity and (b) reconstruct data in regions overwhelmed by noise. Additionally, estimating the field maps from a separate scan is often inaccurate due to the estimate itself being warped and, due to its dependence on subject motion and dynamic changes with physiological conditions [18]. Recently, one method [19] was proposed in the literature which suggests the joint estimation and correction of distortion artifacts via a slight modification to EPI. However, similar to most processing-based techniques, the performance of this approach is inherently limited by signal loss. In this work, we advocate a more universal approach that relies on the joint design of the acquisition method

This work has been supported in part by NIH grant T32MH015442 and in part by the University of Colorado's Developmental Psychobiology Endowment Fund.

J. Dagher is with the Institute of Cognitive Science, University of Colorado, Boulder, CO, USA and with the Brain Imaging Center, University of Colorado, School of Medicine, Denver, CO, USA joseph.dagher@colorado.edu

F. Meyer is with the department of Electrical Engineering, University of Colorado, Boulder, CO, USA fmeyer@colorado.edu

and corresponding reconstruction algorithm. Specifically, we propose a practical multi-acquisition method that captures EPI data in a diverse fashion. An optimally adapted reconstruction algorithm estimates the field map that best explains the diverse measurements and reconstructs a MMSE estimate of the original object. The diversity of the measurements allows us to reconstruct the object, even in cases of severe signal loss. This novel paradigm also generates an estimate of the field maps, without any prior knowledge about the field maps. The rest of the paper is organized as follows. Section II presents the forward imaging model and introduces the problem. We propose one solution in Section III-B, and present the corresponding simulation results in Section IV and concluding remarks and future work in Section V.

II. THEORY

A. Image formation forward model

In this section, we present the forward model which describes the 2D image formation process in EPI. Starting from (1), and using the discrete spatial frequency sampling of EPI, $(K_x(t) = m\Delta k_x, K_y(t) = n\Delta k_y)$, $-N_x/2 \leq m \leq N_x/2$,$-N_y/2 \leq n \leq N_y/2$, we can can write the signal from the selected slice as

$$S[m\Delta k_x, n\Delta k_y] = \int_{-\Delta Z/2}^{\Delta Z/2} \mathrm{d}z \iint f(x,y) \exp\Big\{ i2\pi \big[m\Delta k_x x + n\Delta k_y y + \gamma\!\!\!^{-}\Delta B(x,y,z)t \big] \Big\} \mathrm{d}x\mathrm{d}y, \quad (2)$$

where ΔZ is the slice thickness and t is the sampling time for EPI given by $t = \mathrm{TE} + m\Delta t + nT$, TE is the echo time, Δt is the dwell time, and T is the time between two consecutive phase-encode lines n. Going from (1) to (2), we have approximated $f(x,y,z,t)$ with $f(x,y,z=0)$ and ignored $T1/T2$ relaxation effects. We have also reasonably assumed that the function ΔB is slowly varying compared to the data acquisition window. The spatial variation of ΔB, however, is more complicated and is determined by the underlying sources of inhomogeneities. In this paper, we consider the following model for the inhomogeneity term:

$$\Delta B(x,y,z) \approx g_0(x,y) + g_1(x,y)z, \quad (3)$$

where we expanded $\Delta B(x,y,z)$ in z, with $g_0(x,y)$ and $g_1(x,y)$ being the zeroth and first order Spatially-varying Inhomogeneity Coefficients (SIC), respectively. The model in (3) takes into account both, in-plane field inhomogeneities, $g_0(x,y)$, and any susceptibility-induced field gradients across the slice-selective z direction, $g_1(x,y)$. The majority of existing inhomogeneity correction methods only consider one of these terms at a time. Methods that focus on correcting $g_0(x,y)$-related artifacts, such as pixel shift and region deformation, use signal processing methods to unwarp the images using estimates of $g_0(x,y)$ obtained via field maps. On the other hand, methods aiming to correct $g_1(x,y)$-related signal losses, which could be very severe, generally use signal acquisition methods to recover the signal intensity in a localized region [14]. In this paper, we aim to correct for both artifacts using a joint acquisition-processing scheme.

Replacing (3) in (2) and integrating over z, we can then write the resulting $N_x \times N_y$ discretized measurements as:

$$\begin{aligned} S[m,n] = \iint & f(x,y) e^{i2\pi[m\Delta k_x x + n\Delta k_y y]} \\ & e^{i2\pi\gamma\!\!\!^{-} g_0(x,y)(\mathrm{TE}+m\Delta t+nT)} \\ & \mathrm{sinc}\left[\pi\gamma\!\!\!^{-}\Delta Z g_1(x,y)(\mathrm{TE}+m\Delta t+nT)\right] \mathrm{d}x\mathrm{d}y. \end{aligned} \quad (4)$$

Reconstructing $f(x,y)$ from the discrete samples $S[m,n]$ is a challenging task. In this paper, we make the reasonable assumption that we are only interested in reconstructing $f(x_p, y_q)$ on the discrete sampling grid defined by the EPI sequence. Furthermore, we assume that the object and the SIC terms do not vary considerably inside the rectangular pixel. It can be shown that this latter assumption allows us to re-write (4) as:

$$\begin{aligned} S[m,n] = \sum_{p=0}^{N_x-1} \sum_{q=0}^{N_y-1} & f(x_p,y_q) e^{i2\pi\left[\frac{mp}{N_x}+\frac{nq}{N_y}\right]} \\ & e^{i2\pi\gamma\!\!\!^{-} g_0(x_p,y_q)(\mathrm{TE}+m\Delta t+nT)} \mathrm{sinc}\Big(\frac{m}{N_x}\Big)\mathrm{sinc}\Big(\frac{n}{N_y}\Big) \\ & \mathrm{sinc}\left[\pi\gamma\!\!\!^{-}\Delta Z g_1(x_p,y_q)(\mathrm{TE}+m\Delta t+nT)\right], \end{aligned} \quad (5)$$

where we have used $x_p\Delta k_x = p/N_x$ and $y_q\Delta k_y = q/N_y$ and where the additional sinc terms arise due to the grid of rectangular pixels. Equation (5) describes the forward model for 2D EPI image formation, as corrupted by SIC in (3). The transformation which maps f at (x_p, y_q) into S at (m,n) is a 4D matrix. We can substantially simplify this tensor relationship by observing that $\Delta t << T$, which implies that the SIC would have strong effects only along the y direction. This fact is exploited in most EPI distortion correction techniques [14]. Using some matrix manipulations, we can show that the m^{th} row in (5), $\mathbf{S}_m$, can be written as:

$$\mathbf{S}_m = \mathrm{sinc}(m/N_x) \sum_p e^{i2\pi\frac{mp}{N_x}} \mathbf{s}_{x_p}. \quad (6)$$

$\mathbf{s}_{x_p}$ is a $1 \times N_y$ vector given by

$$\mathbf{s}_{x_p} = \mathbf{f}_p \mathbf{H}_{x_p}, \quad (7)$$

where $\mathbf{f}_p$ is the p^{th} row of the object, and $\mathbf{H}_{x_p}$ is the $N_y \times N_y$ forward model matrix, mapping the spatial index y_q to its conjugate index n, for each x_p, and is given by

$$\begin{aligned} H_{x_p}(y_q,n) = & e^{i2\pi\frac{nq}{N_y}} e^{i2\pi\gamma\!\!\!^{-} g_0(x_p,y_q)(\mathrm{TE}+nT)} \mathrm{sinc}(n/N_y) \\ & \mathrm{sinc}\left[\pi\gamma\!\!\!^{-}\Delta Z g_1(x_p,y_q)(\mathrm{TE}+nT)\right]. \end{aligned} \quad (8)$$

We have thus transformed the 4D tensor forward model of (5) into N 2D forward model matrices. This will reduce the complexity of the model without sacrificing its accuracy.

Finally, no realistic imaging model is complete without taking noise into consideration. We thus write the measurement as the sum of the signal in (7) and a noise term $\mathbf{w}_p$, namely:

$$\mathbf{m}_p = \mathbf{f}_p \mathbf{H}_{x_p} + \mathbf{w}_p. \quad (9)$$

B. Problem statement

We see from (6) that $\mathbf{s}_{x_p}$ is the p^{th} row of a matrix obtained by taking the inverse 1D Discrete Fourier Transform (DFT) across the rows of the matrix formed by stacking the row vectors $(\text{sinc}(m/N_x))^{-1}\mathbf{S}_m$, $m = 1, \ldots, N_x$. Thus, by solving (7), we can then reconstruct the p^{th} row of the object from the vector $\mathbf{s}_{x_p}$. Only a few methods in the literature attempt to correct for fMRI distortion via similar linear systems formulation [16], [20], [21]. The lack in popularity of this approach is due to two obstacles. First, in the presence of noise, inverting $\mathbf{H}_{x_p}$ in (7) will yield highly unstable solutions. This is particularly true in regions with low signal, which is the case when the value of $g_1(x_p, y_q)$ is large. The authors in [16] address this difficulty by separating $\mathbf{H}_{x_p}$ into two matrices: one corresponding to $g_1(x_p, y_q)$ effects and the second includes the remaining effects. Then, the authors invert the matrix due to $g_1(x_p, y_q)$ using truncated iterative methods, thus reducing the effects of noise amplification. The method in [16] is therefore unable to fully reconstruct the signal in regions with large $g_1(x_p, y_q)$. The second obstacle with the linear systems approach is that $\mathbf{H}_{x_p}$ and $\mathbf{f}_p$ are both unknown. The authors in [16] make the common assumption that $g_0(x_p, y_q)$ and $g_1(x_p, y_q)$ do not change over the entire scan period and use a separate measurement at the beginning of the scan to get an estimate of these quantities. As pointed out in Section I, this assumption is not realistic. The reconstruction problem thus falls under the class of parameterized blind signal deconvolution [22]. Standard methods used to estimate $\mathbf{H}_{x_p}$ and $\mathbf{f}_p$ become unreliable at low signal to noise ratios. As an example, Fig. 1 illustrates different profiles of $\mathbf{H}_{x_p}$ at typical values of $g_1(x_p, y_q)$: in the Orbito-Frontal cortex g_1 is reported to be on the order of $0.2-0.3$ mT/m at 3T [12]. We note immediately the low value of the response around $K_y = 0$. This implies that the corresponding measurement will be dominated by noise and that processing-based techniques for estimating the forward model matrix $\mathbf{H}_{x_p}$ will be not be robust. In this paper, we offer a joint acquisition-reconstruction method to solve the following problems: (a) estimate the SIC (or, $\mathbf{H}_{x_p}$) without using any prior knowledge and, (b) obtain a Linear MMSE (LMMSE) reconstruction of the object, $\mathbf{f}_p$, $\forall p$. Hereafter, and for simplicity, we consider only one row in our discussion and drop all x_p and p indices from (9). Our simulation results, naturally, will include all rows.

III. JOINT ACQUISITION-RECONSTRUCTION

A. Formulation

In order to solve the problems presented above, we advocate using a joint acquisition-processing approach. The proposed method does not require prior-knowledge of the field maps $\Delta B(x, y)$. The general approach consists of the following three steps **S1**, **S2** and **S3**:

(**S1**) Acquire K measurements at different points in time $\{\mathbf{m}_1, ..., \mathbf{m}_K\}$, each given by

$$\mathbf{m}_k = \mathbf{f}\,\mathbf{H}_k(\mathbf{g}) + \mathbf{w}_k, \tag{10}$$

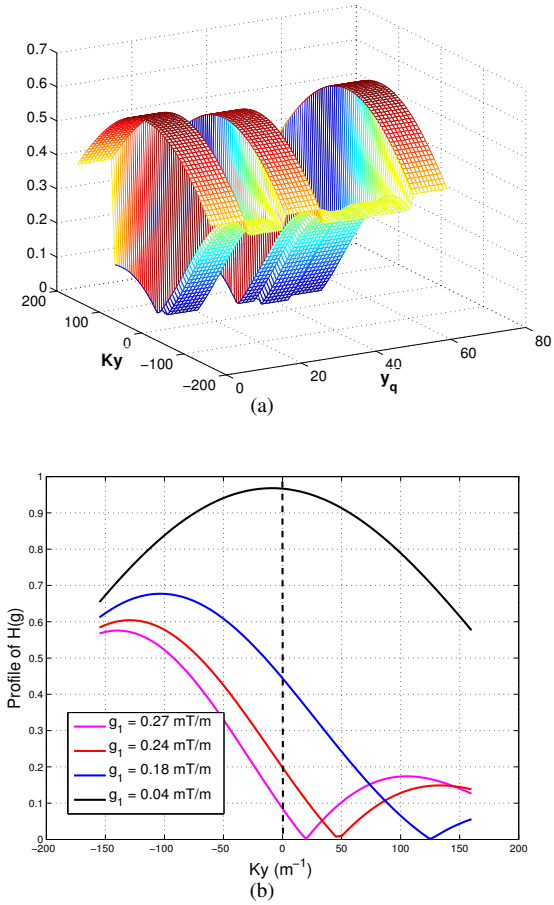

Fig. 1. (a) The magnitude of $\mathbf{H}_{x_p}$, for $p = 32$, shown as a function of y_q and K_y for common EPI acquisition parameters. For a given y_q (and hence $g_0(x_p, y_q)$ and $g_1(x_p, y_q)$), the profile represents the response as a function of spatial frequency K_y. Example profiles are shown in (b). Note the low response around $K_y = 0$, yielding signal drop and reconstruction difficulty in the presence of noise. Recall that the profile does not change significantly with K_x.

where $\mathbf{H}_k(\mathbf{g})$ represents the forward model matrix associated with the k^{th} acquisition which is related to the underlying forward model matrix $\mathbf{H}$ of (8) by

$$\mathbf{H}_k(\mathbf{g}) = \mathcal{T}_k(\mathbf{H}; \mathbf{g}) \tag{11}$$

for $k = 1, \ldots, K$. $\mathcal{T}_k$ is a carefully chosen transformation with specific properties discussed below. This is the only required change in acquisition. We present one example transformation in Section III-B. Note that $\mathcal{T}_k$ is clearly a function of $\mathbf{g}$, the vector of SIC terms.

(**S2**) Using the K measurements $\{\mathbf{m}_1, ..., \mathbf{m}_K\}$, we estimate the underlying SIC $\mathbf{g}$ to be the vector which best explains measurement $\mathbf{m_j}$, given $\mathbf{m_i}$, $\forall i$. That is,

$$\widehat{\mathbf{g}} = \underset{\mathbf{g}}{\text{argmin}} \sum_{1 \le j \le K} \left\| \widehat{\mathbf{f}}[\widetilde{\mathbf{m}}; \mathbf{g}]\, \mathbf{H}_j(\mathbf{g}) - \mathbf{m}_j \right\|^2, \tag{12}$$

where $\widetilde{\mathbf{m}}$ is the concatenated K-channel measurement vector and $\widehat{\mathbf{f}}[\widetilde{\mathbf{m}}; \mathbf{g}]$ is an estimate of the object reconstructed from all the measurements $\widetilde{\mathbf{m}}$, assuming the actual SIC is given

by $\mathbf{g}$. This object estimate is computed using step **S3** below.
(**S3**) Given an estimate of $\mathbf{g}$, compute the set of K forward model matrices $\mathbf{H_k}$, and reconstruct an estimate of the object $\widehat{\mathbf{f}}$ using multi-channel deconvolution formulation [22],

$$\widehat{\mathbf{f}}[\widetilde{\mathbf{m}};\widehat{\mathbf{g}}] = \underset{\mathbf{f}}{\operatorname{argmin}} \left\| \widetilde{\mathbf{m}} - \mathbf{f}\mathbf{H}_{\mathbf{1:K}}(\widehat{\mathbf{g}}) \right\|^2 + \lambda J(\mathbf{f}), \qquad (13)$$

where $\mathbf{H_{1:K}}$ is the concatenation of the K-channel forward model matrices, estimated assuming SIC distribution $\widehat{\mathbf{g}}$. $J(\mathbf{f})$ is a regularization term.
Steps (**S1**)-(**S3**) above, along with (11), (12) and (13) define what we refer to hereafter as the Multi-acquisition Blind Estimation and Reconstruction (MBER) approach. We note the following important remarks:

(a) Because we now acquire K images instead of one, we will need to sacrifice quality (e.g., SNR, resolution) in each measured image $\mathbf{m}_k$ in order to keep the acquisition time constant. This penalty term is included in each $\mathbf{H}_k$ and is a function of K and $\mathcal{T}_k$.
(b) We advocate that the choice of $\mathcal{T}_k$ should satisfy the following two properties:
Property P1: The set of matrices $\{\mathbf{H}_k\}$ should result in diverse measurements of $\mathbf{f}$. Intuitively, this can be motivated by the following observation: if all $\mathbf{H}_k$ were similar, i.e. minimally diverse, then this compromises our ability to discriminate measurements, and hence the estimation step (12) is adversely affected.
Property P2: The matrices should yield measurements with a quality metric larger than the underlying noise level. Indeed, a non-careful choice of the $\{\mathbf{H}_k\}$ may yield measurements that are dominated by noise. This negatively affects the reconstruction step (13).
(c) Equations (12) and (13) define a truly joint estimation-reconstruction approach for computing SIC terms and recovering the object. The formulation uses an L_2 metric in both equations. However, other metrics could easily be adopted, including $L1$ norm (in estimation), probability of detection, classification performance (in reconstruction).
(d) Equations (11), (12) and (13) are the foundation for a joint acquisition-reconstruction paradigm. These equations define a unifying framework which can be used to jointly optimize acquisition and processing parameters for minimizing distortion artifacts in EPI.

In this work, we propose one acquisition method $\mathcal{T}_k$, and a corresponding reconstruction algorithm, and compare its performance to traditional inhomogeneity correction methods.

B. Acquisition method

We describe here one multi-acquisition method associated with step (**S1**) of Section III-A above.

It is obvious from estimation step (**S2**), and property Property *P1*, that we desire a transformation which modulates the SIC terms in (8) so as to generate a diverse set of measurements. We propose one such transformation $\mathcal{T}_k$:

$$\mathcal{T}_k(\mathbf{H})_{(\mathbf{g})} = e^{i2\pi \frac{nq}{N_y}} e^{i2\pi \not{\gamma} g_0(x_p,y_q)(\mathrm{TE}_k + nT)} \mathrm{sinc}(n/N_y) \quad (14)$$
$$\mathcal{M}_K \mathrm{sinc}\left[\pi \not{\gamma} \Delta z \left(g_1(x_p,y_q)(\mathrm{TE}_k + nT) - g_{ck}\tau_c\right)\right]$$

where $\mathcal{M}_k$ denotes a magnitude penalty term, TE_k denotes the value of the k^{th} echo time and g_{ck} is a compensation gradient introduced during the k^{th} acquisition, for a period of time τ_c. It is clear from the form of (14) that the set of compensation gradients $\{g_{ck}\}$ can be used to shift the sinc around, and thus modulate the $g_1(x_p,y_q)$ term and $\mathbf{H}_k$. This also has the effect of modulating the magnitude of the measurements $\mathbf{m}_k$. Similarly, the variable echo time TE_k can be used to modulate the $g_0(x_p,y_q)$ term, $\mathbf{H}_k$, and the phase of $\mathbf{m}_k$. The pulse sequence which generates such a forward model matrix is essentially a variable echo time "z-shim" sequence [11], whereby a known gradient area is introduced along the z-direction during acquisition, each at a given echo time. This is repeated K times for each slice of interest. Associated with this multi-acquisition is a trade-off for acquiring $K-1$ additional measurements. In other words, the z-shim pulse sequence should be designed to keep the imaging time constant. This could be achieved via the reduction of the number of samples captured ("under-sampling" of the FOV), increasing the scan bandwidth (if possible), reducing the number of imaged slices, etc. In this paper, we adopt a z-shim protocol whereby a reduced number of distinct slices per volume is acquired during the same Repetition Time TR. It can be shown that the penalty term associated with this trade-off is an exponential reduction in measurement SNR as a function of K (see (15)). The reason for this decay is due to the fact that the slice of interest is now acquired (excited) K times during the same TR (i.e., partial saturation). We refer the reader to [23] for more details on the sequence. Namely, when the data is acquired with a flip angle equal to Ernst angle of gray matter, the magnitude of $\mathbf{H}_k$ is reduced by a factor $\mathcal{M}_K$, given by

$$\mathcal{M}_K = \mathcal{M}_0 \sqrt{\frac{1 - e^{-\mathrm{TR}/\mathrm{T1}K}}{1 + e^{-\mathrm{TR}/\mathrm{T1}K}}}, \qquad (15)$$

where T1 is the relaxation constant of gray matter and $\mathcal{M}_0$ is the maximum available magnetization [23].

According to properties *P1* and *P2* from Section III-A, the choice of the set of compensation gradients $\{g_{ck}\}$ and the set of echo times $\{\mathrm{TE}_k\}$ is crucial to the performance of the MBER method. In fact, the choice of $\{g_{ck}\}$ and $\{\mathrm{TE}_k\}$ could be optimized to guarantee a given reconstruction performance. Our paradigm enables us to readily tackle such a problem. This is beyond our scope here. In this paper, we choose the $\{g_{ck}\}$ and $\{\mathrm{TE}_k\}$ to be uniformly spaced on a pre-defined range of interest. Specifically, we choose the echo times uniformly between 20ms and 30ms, with steps of $\frac{1}{100}$s. We can show via mathematical manipulations that this chosen step size would guarantee the estimation of g_0 terms that are in the range of ± 100Hz. The compensation gradients are chosen in the range ± 9 mT ms/m, carefully chosen to

correct for g_1 terms that are in the range of $\pm 300\mu$T/m. We assume a 3T main magnetic field in our simulations.

Finally, we note here that one important novelty of our work is the joint acquisition-reconstruction framework, introduced in Section III-A, which exploits the acquisition diversity in order to reconstruct the object. The modification to the EPI pulse sequence we presented here is one example multi-acquisition sequence which can be quickly used to generate such diverse acquisitions. Other modifications, with different diverse multi-acquisition strategies and corresponding trade-off space, could be proposed. This is one very important advantage of our paradigm.

C. Corresponding reconstruction method

We use our implementation of an adaptive Simulated Annealing algorithm to numerically solve (12). Then, we reconstruct the object using an implementation of the Landweber iterative algorithm. The reconstruction-estimation steps are iteratively repeated until a stopping criteria is reached. We direct the reader to standard signal reconstruction references for more information on this topic [22], [24]. We should point out here that we expect our iterative inversion of the multi-channel matrix $\mathbf{H_{1:K}}$ to be less susceptible to noise amplification. The reason for this is that we are acquiring K measurements, each of which generated by a forward model matrix with a differently shifted sinc (14). Thus, a given region with large $g_1(x_p, y_q)$ is less likely to suffer from complete signal loss in all K measurements, as compared to methods which only acquire one measurement. This will overcome the need to implement complicated inversion method such as the one reported in [16].

IV. SIMULATION RESULTS

We report in this section the results of our simulations. Fig. 4a illustrates the proton density of an object with zeroth and first order SIC terms shown in Figs. 4b and 4c, respectively. The chosen range of SIC is shown on the color bar. We use this object to simulate a standard EPI acquisition. The result is shown in Fig. 4d. We note the typical EPI artifacts reproduced here, including geometric deformation and signal drop around regions in the image. The Signal-to-Noise Ratio (SNR) was set here to a typical value of 40dB. Figure 4e illustrates the result of a second acquisition, obtained using the uniform z-gradient and TE stepping described in the previous section. Note that the top ellipse is now brighter while the ellipse on the right suffered from a signal drop. This is an expected behavior of z-shimming which corrects for artifacts in one region of the image at the expense of others. We argue that, in order to obtain a fair comparison, we only should consider methods that do not require prior knowledge nor a separate measurement of field maps. One such method is the established SSQ algorithm [11], [23]. SSQ collects multiple z-shimmed measurements of the object with carefully chosen and calibrated z-compensation gradients [12] and, combines the measurements using the root sum of the magnitudes squared. Unlike our method, SSQ needs a careful calibration step in order to choose the z-gradient steps. Our multi-acquisition approach uniformly picks the compensation steps over a pre-defined range of interest. Fig. 4f displays the output of SSQ using $K = 3$ measurements. The corresponding RMSE of the reconstructed object is 69. Note that signal drop persists in many portions of the image. Also, as expected, we see that SSQ is unable to correct for geometric warping in the image. Fig. 4g shows the object reconstructed using our MBER method, yielding an RMSE of 23. We note that our method was able to fully recover the signal in all regions, as well as correct for geometric warping. The resulting drastic improvement in visual quality is reflected by a reduction in the RMSE by a factor of 3. The RMSE may not be the most suitable metric that best reflects such dramatic improvement in quality. Nevertheless, we continue to use it hereafter for conciseness. Next, recall that our method also blindly estimates the SIC terms. Figs. 4h and 4i show the estimated SIC maps. Note the impressive accuracy of the estimates, when compared to Figs. 4b and 4c. This demonstrates an additional advantage of our approach: we can efficiently recover the spatial distribution of the inhomogeneity coefficients, or field maps. Finally, in order to gauge the performance of the reconstruction algorithm more carefully, we implemented a "genie" version of our approach. We assume that this genie has perfect knowledge of the SIC distribution, $g_0(x_p, y_q)$ and $g_1(x_p, y_q)$. Fig. 4j shows the result of our multi-channel reconstruction had the estimation step been perfect. The impressive quality (RMSE=0.5) of the resulting object estimate, which was derived from images such as those shown in Figs. 4d and 4e, implies that our reconstruction method (13) is capable of completely correcting the object, even in regions with low SNR and large amount of warping, without yielding any artifacts. This is not possible with existing methods in the literature [16]. This also implies that better SIC estimation methods are worth investigating as they dramatically improve the quality of the reconstruction. Our completely blind estimation step is the best we can achieve, in the MMSE sense. However, the accuracy of the SIC estimates could be improved by incorporating some prior-knowledge about its distribution. This is beyond our scope here.

We have illustrated the gain in performance obtained using our algorithm for a given K and SNR. Next, we vary the SNR level and repeat the process described above for various SIC distributions and noise realizations (sampled from a white Gaussian process). We then report the average RMSE in the reconstructed object magnitude as a function of SNR in Fig. 2 for $K = 2, 3$ and 4. The blue and black curves represent the performance of the MBER algorithm and the SSQ method, respectively. The red lines implements the genie-driven MBER algorithm, which reports the lower bound on the reconstruction performance. The case of $K = 2$ is represented with a solid line, $K = 3$ with a dashed line and $K = 4$ with a triangle-marked dashed line. We note the following: first, the MBER algorithms exhibit a decrease of RMSE with SNR. This is expected and is a typical trend in noise-dominated regimes. On the other hand, SSQ reconstructions are in a blur-dominated regime: the contribution

to the RMSE from the degradation (blur) operator outweighs that from additive noise, at all SNRs. This explains the constant performance we observe with this method. Second, we see that MBER achieves a large reduction in RMSE as compared to SSQ at all SNRs. For example, for $K = 4$ and SNR=35dB, we see that MBER reduces the RMSE by an impressive factor of 5, as compared to SSQ. Finally, note the outstanding reconstruction performance of genie-MBER, as promised by an optimal estimation method. Finally, we answer the following very important question: what is the optimal number of measurements K we should make, from an MMSE perspective, for this specific choice of multi-acquisition strategy defined in Section III-B? As noted earlier, any multi-acquisition method has a magnitude penalty term associated with additional acquisitions. So we expect a performance "roll-over" after a number of measurements. We answer this in Fig. 3 where we plot RMSE vs K at SNRs of 40dB (solid line) and 30dB (dashed line) for the MBER algorithm (blue line) and SSQ method (black line). Note the log-scale used for the vertical axis. We can see that the optimal performance of the MBER method is reached around $K = 5$ measurements, yielding an improvement in RMSE by an outstanding factor of 5.2 at 30dB and 7.7 at 40dB as compared to SSQ.

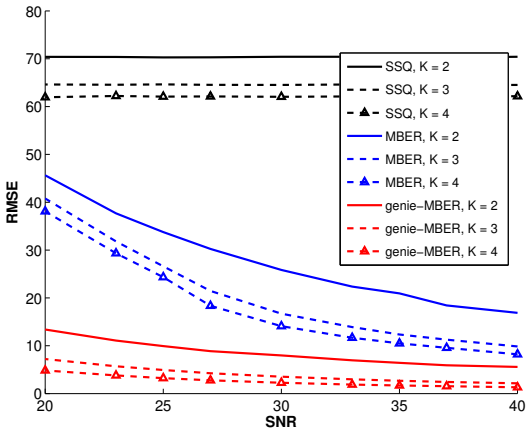

Fig. 2. The RMSE in the reconstructed object as a function of SNR (dB) is shown for $K = 2$, $K = 3$ and $K = 4$. Note the tremendous gain in our suggested MBER (blue line) approach over the SSQ method (black line). The red line shows the lower bound that can be achieved via perfect knowledge of the SIC terms.

V. Conclusion and Future Work

We have presented here a novel joint acquisition-processing paradigm for reconstructing fMRI data corrupted by inhomogeneity artifacts. This paradigm explores a novel solution space for this very important problem. We have proposed one practical implementation of this paradigm. Specifically, we proposed a multi-acquisition method which captures diverse correlated views of the same slice by applying K z-compensation gradients at K echo times, both uniformly sampled over a range of interest. We then designed a corresponding joint estimation-reconstruction algorithm.

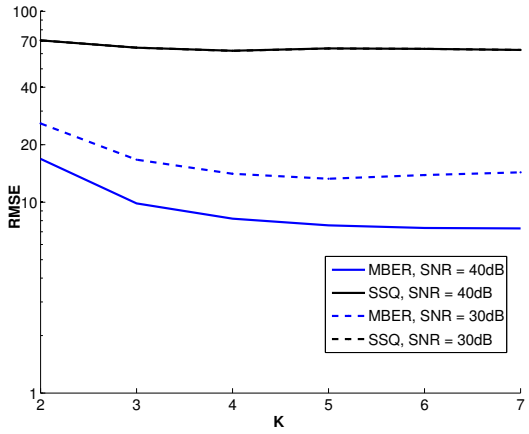

Fig. 3. Performance of MBER (blue) as a function of K for typical SNR values of 40dB and 30 dB, suggesting an optimal number of 5 acquisitions. Note the impressive gain over SSQ (black lines).

The estimation method is capable of calculating a map of the inherent SIC terms which explain the captured data the most, from an MMSE sense. This estimation step is a powerful tool which can be used as a robust field mapping routine. The method does not require any prior knowledge of the field maps. The reconstruction method uses the information computed by the estimation routine, along with the measurements, in order to derive a MMSE estimate of the object. The reconstruction-estimation steps are iteratively repeated until a stopping criteria is reached. Our simulation results show an expected reduction in RMSE by a factor as high as 7.7, as compared to other established methods that do not require prior knowledge of the field maps. Even in cases of severe signal loss, the reconstruction method is able to combine the diverse measurements and recover the signal in the affected regions. This is a major advantage over existing methods which are limited by the SNR level across the image [16]. Future work includes the immediate evaluation of the efficiency of our proposed method *in-vivo*. Also, we note that the slight modification to the EPI pulse sequence we presented here is one example of an acquisition strategy which can generate diverse acquisitions. Other modified EPI sequences and corresponding diverse acquisition strategies, albeit with different tradeoffs, will be explored. Finally, we note that one very important advantage of our formulation is the ability to jointly optimize the transformation $\mathcal{T}_j$ along with the reconstruction performance. In fact, one immediate example would be to optimize the choice of the compensation gradients and echo times so as to maximize reconstruction performance.

VI. Acknowledgments

The authors would like to thank Prof. Brad P. Sutton for his suggestions.

References

[1] M. Haacke, R. Brown, M. Thompson, and R. Venkatesan, Magnetic resonance imaging: physical principles and sequence design. Wiley-Liss, 1999.

[2] P. Jezzard and S. Clare, "Sources of distortion in functional MRI data," Human Brain Mapping, vol. 8, pp. 80–85, 1999.

[3] P. Jezzard and R. Balaban, "Correction for geometric distortion in echo planar images from B_0 field variations," Magnetic Resonance in Medicine, vol. 34, 1995.

[4] B. Sutton, C. Ouyang, and D. Karampinos, "Current trends and challenges in MRI acquisitions to investigate brain function," International Journal of Psychophysiology, vol. 73, pp. 33–42, 2009.

[5] J. Ashburner, P. Neelin, D. Collins, A. Evans, and K. Friston, "Incorporating prior knowledge into image registration," Neuroimage, vol. 6, pp. 344–352, 1997.

[6] A. Gholipour, N. Kehtarnavaz, R. Briggs, M. Devous, and K. Gopinath, "Brain functional localization: A survey of image registration techniques," IEEE Transactions on Medical Imaging, vol. 26, pp. 427–451, 2007.

[7] P. Matthews, G. Honey, and E. Bullmore, "Applications of fMRI in translational medicine and clinical practice," Nature reviews, Neuroscience, vol. 7, no. 9, pp. 732–744, 2006.

[8] G. Feigl, S. Safavi-Abbasi, A. Gharabaghi, V. Gonzalez-Felipe, A. E. Shawarby, H. Freund, and M. Samii, "Real-time 3T fMRI data of brain tumour patients for intra-operative localization of primary motor areas." European journal of surgical oncology, vol. 34, no. 708-715, 2008.

[9] R. Gruetter, "Localized in vivo adjustment of all first and second-order shim coils," Magnetic Resonance Imaging, pp. 801–811, 1993.

[10] Y. Zhao, A. Anderson, and J. Gore, "Computer simulation studies of the effects of dynamic shimming on susceptibility artifacts in EPI at high field," Magnetic Resonance Imaging, vol. 173, pp. 10–33, 2005.

[11] R. Constable and D. Spencer, "Composite image formation in z-shimmed functional MR imaging," Magnetic Resonance in Medicine, vol. 1, no. 42, pp. 110–117, 1999.

[12] D. Cordes, P. Turski, and J. Sorenson, "Compensation of susceptibility-induced signal loss in echo-planar imaging for functional applications," Magnetic Resonance Imaging, vol. 9, pp. 1055–1068, 2000.

[13] N. Chen and A. Wyrwicz, "Correction for EPI distortions using multi-echo gradient-echo imaging," Magnetic Resonance in Medicine, vol. 41, pp. 1206–1213, 1999.

[14] C. Hutton, A. Bork, O. Josephs, R. Deichmann, J. Ashburner, and R. Turner, "Image distortion correction in fMRI: A quantitative evaluation," Neuroimage, vol. 16, pp. 217–240, 2002.

[15] M. Zaitsev, J. Hennig, and O. Speck, "Point spread function mapping with parallel imaging techniques and high accelation factors: Fast, robust and flexible method for echo-planar imaging distortion correction," Magnetic Resonance in Medicine, vol. 52, pp. 1156–1166, 2004.

[16] G. Liu and S. Ogawa, "EPI image reconstruction with correction of distortion and signal losses," Journal of Magnetic Resonance Imaging, vol. 24, no. 3, pp. 683–689, Jan 2006.

[17] G. Tao, R. He, A. Poonawalla, and P. Narayana, "Nonlinear image registration with voxel adaptive regularization to correct for EPI-induced geometric distortions," in ISMRM, 2007, p. 986.

[18] N. kuei Chen, K. Oshio, and L. P. Panych, "Application of k-space energy spectrum analysis to susceptibility field mapping and distortion correction in gradient-echo EPI," NeuroImage, vol. 31, no. 2, pp. 609–22, Jun 2006.

[19] H. Nguyen, B. Sutton, R. M. Jr, and M. Do, "Joint estimation and correction of geometric distortions for EPI functional MRI using harmonic retrieval," IEEE Transactions on Medical Imaging, vol. 3, no. 28, pp. 423–434, 2009.

[20] Y. Kadah and X. Hu, "Algebraic reconstruction for magnetic resonance imaging under B0 inhomogeneity," IEEE Transactions on Medical Imaging, vol. 17, pp. 362–370, 1998.

[21] P. Munger, G. Crelier, and T. Peters, "An inverse approach to the correction of distortion in EPI images," IEEE Transactions on Medical Imaging, vol. 19, pp. 681–689, 2000.

[22] A. C. Bovik, Ed., Handbook of Image and Video Processing. Academic Press, 2000.

[23] Y. Du, M. Dalwani, K. Wylie, E. Claus, and J. Tregellas, "Reducing susceptibility artifacts in fMRI using volume-selective z-shim compensation," Magnetic Resonance in Medicine, vol. 57, pp. 396–404, 2007.

[24] H. H. Barrett and K. J. Myers, Foundations of Image Science. Wiley-Interscience, 2003.

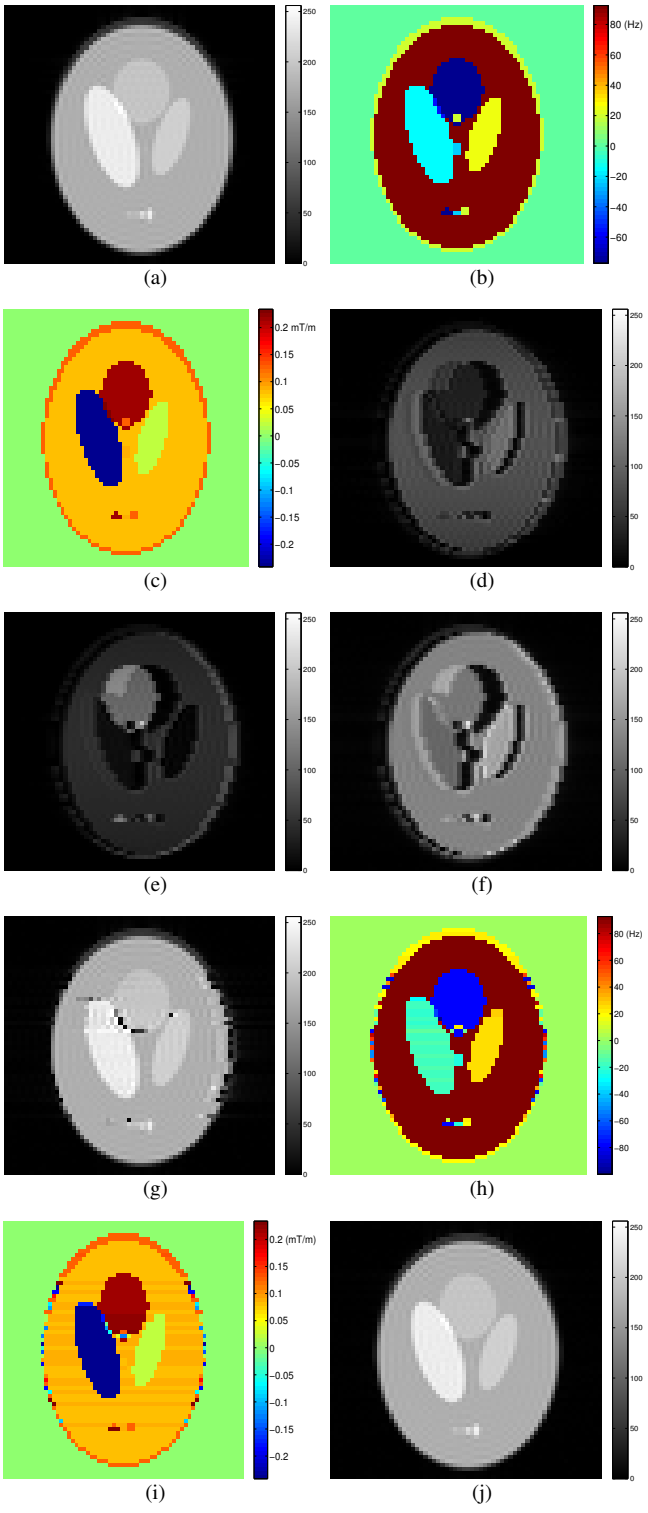

Fig. 4. (a) Original object density possessing the (b) $g_0(x_p, y_q)$ and (c) $g_1(x_p, y_q)$ distribution maps. This yields a typical EPI measurement shown in (d). $K = 3$ measurements were collected according to the multi-acquisition protocol described in Section III-B, one example of which is shown in (e). Note the change in intensity distribution as compared to (d). The object was reconstructed using (f) the SSQ method (RMSE=69) and (g) our MBER framework (RMSE=23). The zeroth and first order SIC maps estimated by MBER are shown in (h) and (i), respectively. Finally, (j) shows the estimated object had we had perfect knowledge of the SIC terms (RMSE=0.5).